Quantitative biomarkers allow the diagnosis of head and neck paraganglioma on multiparametric MRI

Eric Guedj, Françoise Lazarini, Silvia Morbelli, Mathieu Ceccaldi, Charlotte Hautefort, Aurélie Kas, Thomas Radulesco, Dominique Salmon-Ceron, Carole Eldin, Jacob Bani, et al.

Quantitative biomarkers allow the diagnosis of head and neck paraganglioma on multiparametric MRI

Emina Arsovic[1], Marion Montava[2], Nicolas Fakhry[2], Jean-Pierre Lavieille[2], Karel Pacak[3], David Taïeb[1*], Arthur Varoquaux[4,5*]

[1]Department of Nuclear Medicine, La Timone University Hospital, CERIMED, Aix-Marseille University, France

[2]Department of Head and Neck Surgery, Conception Hospital, Aix-Marseille Univ, France

[3]Section on Medical Neuroendocrinology, *Eunice Kennedy Shriver* National Institute of Child Health & Human Development (NICHD), National Institutes of Health, Bethesda, Maryland, 20892 USA.

[4]Department of Medical Imaging, Conception University Hospital, Aix-Marseille Univ, France

[5]Center for Magnetic Resonance in Biology and Medicine, UMR 7339, La Timone University Hospital, Aix-Marseille Univ, France

*DT and AV contribute equally to the manuscript

Corresponding author: Arthur Varoquaux, Department of Medical Imaging, Conception University Hospital, Center for Magnetic Resonance in Biology and Medicine, UMR 7339, La Timone University Hospital, Aix-Marseille Univ, France. Email: Arthur.VAROQUAUX@ap-hm.fr, Phone/FAX: +33 (0) 4 91 38 39 03

Abstract

Purpose: The aim of this study is to identify quantitative MR biomarkers in head and neck paragangliomas.

Methods: The study was approved by an institutional review board. A retrospective review of patients with head and neck paragangliomas (HNPGL) evaluated by time-resolved MRA sequences between 2009 and 2019 was performed. A control group investigated during the same period was analyzed, including nerve sheath tumors and metastatic lymph nodes from squamous cell carcinomas or undifferentiated nasopharyngeal cancer (UCNT). A gold standard was obtained for all cases. Semi-quantitative parameters of enhancement were extracted from time-intensity curves on time-resolved MRA sequences and diffusion weighted imaging/DWI was assessed for each lesion.

Results: Sixty head and neck paragangliomas (HNPGLs) were included from 50 patients. The control group consisted of 30 parapharyngeal space lesions (27 patients), which included nerve sheath tumors (n=12) and metastatic lymph nodes (n=18) from squamous cell carcinomas or UCNT. PGLs showed a shorter time-to-peak value compared to other groups, measured at 25.0 +/- 29 sec. The wash-in and wash-out ratios were also significantly higher for PGLs, respectively measured at 5.34 ± 2.99 (p<0,001) and 1.24 ± 0.80 (p<0.001). On DWI sequences, the mean ADC value for PGLs (1.17 ± 0.19 10^-3 mm2/s) was significantly different than the other tumor groups (p<0.001). HNPGLs were clearly distinguishable from other tumors on classification with regression tree based on TTP and ADC values. These distinct group features were also consistent on principal component analysis.

Conclusion: Our study identifies a multiparametric signature for disease subtyping, providing a strong impetus for switching from qualitative to quantitative analysis of deep soft-tissue tumors of the neck.

Key terms : paragangliomas; neck tumors; MRA; DWI; biomarkers; multiparametric imaging

1. Introduction

Head and neck paragangliomas (HNPGLs) are rare neuroendocrine tumors, and represent a subset of pheochromocytoma/paraganglioma (PPGL) neoplasms. HNPGLs are specifically associated with the parasympathetic nervous system, and arise from paraganglia which are derived from multifated Schwann Cell Precursors (SCP) [1,2]. HNPGLs are located close to great vessels and parasympathetic ganglia [3] in middle ear (tympanomastoid PGL), jugular formamen (tympanojugular PGL), retrostyloid parpharyngeal space (vagal PGL), and carotid artery bifurcation (carotid body PGL). HNPGLs have a hereditary background in up to 40% of cases[4]. Of all the known genetic mutations (collectively named SDHx), *SDHD* mutations are currently the leading cause of hereditary HNPGLs [4].

Surgical biopsy of lesions at the base of the skull (e.g. tympanojugular PGL) or located in the vascular space (e.g. vagal PGL) requires complex surgical approaches. Percutaneous biopsy under CT is considered risky because of the proximity of the internal carotid artery and the hypervascular nature of these lesions. Computed tomography (CT) and magnetic resonance angiography (MRA) are conventional tools to depict PGL in the neck with the so-called “salt and pepper” appareance on T2-weighted imaging and tumor hypervascularity on angio-CT imaging. The diagnostic sensitivity of these techniques is relatively low, ranging from 75 to 89% [5,6]. Diffusion-weighted imaging (DWI), which is dependent on tissue cellularity, and DCE witch explores tumors enhancement patterne has both gained a potential role in tumor in differentiating PGL from other deep soft-tissue tumours of the neck [7,8].

The aim of the present study was to identify and to combine quantitative MR biomarkers that allow distinction between paragangliomas and other deep soft-tissue tumours of the neck on DCE and DWI.

2. Materials and methods

2.1 Study population

A comprehensive retrospective automatic search in our database was performed in order to identify all patients evaluated by neck DCE MR imaging and DWI for a presumed PGL from January 2009 to January 2019. A control group evaluated during the same time period was included and comprised of parapharyngeal space squamous cell carcinoma (NSCC) metastatic nodes (n=18 lesions, in 15 patients) and nerve sheath tumors (NSTs, n=12, in 12 patients). Pathological examination was considered the gold standard (level 1 of evidence, n=41). In cases where no surgical resection was performed, the diagnosis of PGL was made by presence of tumor uptake on ^{18}F-DOPA PET (specific radiopharmaceutical). In the remaining cases, the consensus between experienced radiologists and surgeons warranted a diagnosis, where all clinical information, imaging studies and follow-up was taken into account (level 3 of evidence, n=14). The search for SDHx mutations was performed in all PGL, and recorded for further analysis.

2.2 MR imaging

Multiparametric MR imaging data were obtained at 1.5 Tesla (Amira Siemens, Erlangen, Germany) with a 16-channel phased array head and neck coil. DWI and DCE imaging parameters are described in Table 2. Patients first underwent unenhanced DWI, axial T1 weighted sequence without fat suppression, and T2-weighted fast spin-echo. A DCE sequence was then acquired before and during a 0.2 mL/kg gadolinium injection (Dotarem® gadotrial acid, Guerbet France) at 3 ml/sec. An axial and coronal T1WI with fat suppression was performed after gadolinium injection. Three different DCE sequences (gradient-recall-DCE/GRE, spin-echo-DCE/SE or time resolved 4D-MRA/4D) were used in this study,

depending mainly on the indication and inclusion period. GRE, SE and 4D sequences were performed in 26, 24, and 38 lesions, respectively.

2.3 Image analysis

Regions of interest (ROIs) centered on the lesions were manually drawn on DCE images, with exclusion of areas of necrosis. A 10 mm2 OI was placed in consensus by radiologists (E.A. and A.V. with 6 and 20 year of experience in ENT radiology), blinded to clinical report information.

Time-intensity parameters were generated for each ROI using the plugin DCE tool (v2.2) on Horos software (Pixmeo, Bernex, Switzerland, v1.1.17). The following semi-quantitative parameters of enhancement were automatically extracted from time-intensity curves (TICs) for each lesion: basal signal intensity (SI_{pre}), signal intensity at signal peak (SI_{max}), time to peak (TTP), and signal intensity 20 seconds after peak (SI_{20}). Wash in ratio (WIR) and wash out ratio (WOR) were obtained by linear regression of signal intensity, from SI_{pre} to SI_{max} for WIR, and from SI_{max} to SI_{t20} for WOR.

Apparent diffusion coefficient (ADC) maps were calculated with linear regression analysis of the function ln(S/S0) = -b.ADC, where S is the signal intensity after application of the diffusion gradient, S0 is the signal intensity when the b value was 0 sec/mm2 , and b is the b1000 value. The corresponding DCE lesion ROIs were automatically reported on ADC maps.

2.4 Statistical analysis

Statistical analysis and post-processing was performed using the statistical software R (version 3.3.3; R Foundation for Statistical Computing, Vienna, Austria). Univariate analysis consisted of the comparison of quantitative features in each group. Continuous variables were expressed as mean and standard deviation. Comparison of mean values between the two groups were performed using a Student's t-test. ANOVA was used to analyze the differences

among groups in the multivariate analysis. Clusters were obtained by multivariate unsupervised analysis by principal component analysis (PCA) and compared with variables of interest to analyse their relevance. Logistic regression was used in order to build regression diagnostic trees (CART).

3. Results

3.1 Patients, tumors and technical characteristics

A total of 90 tumors (in 77 patients) were evaluated, of which included 60 HNPGLs (10 carotid body PGLs, 16 vagus nerve PGLs, and 34 jugular PGLs), 12 NSTs (11 schwannomas and 1 neurofibroma), and 18 metastatic lymph nodes from squamous cell carcinomas or UCNT. **Table 1** describes characteristics of the lesions, including the gold standard and DCE MRI method that were used across all tumor types. PGLs were histologically proven in 28%. In the remaining cases, PGL diagnosis was based on tumor ^{18}F-DOPA uptake. 48% of HNPGLs were related to a germline mutation in one of the SDH genes (*SDHB*, n=4 in 4 patients; *SDHC*, n=3 in 3 patients; *SDHD*, n= 22 in 13 patients). For NSCC, histological proof was obtained in 33%. **Table 2** describes the imaging parameters of DCE-MRI protocols.

3.2 Dynamic contrast enhancement pattern

All PGLs exhibited early and intense enhancement following gadolinium administration (with a rapid wash-out) on time intensity curves. In contrast, NSTs and NSCCs showed a more progressive enhancement, with a plateau phase. **Figure 1** shows typical time-intensity curves for PGL, NST, and NSCC.

3.3 Univariate analysis

Figure 2 depicts the values of all biomarkers for each tumor type. **Table 3** shows the results of the univariate analysis. All biomarkers were different across the 3 histological tumor types on univariate analysis, with a p-value <0.001. PGLs showed a shorter time-to-peak intensity (TTP) compared to other groups, measured at 25.0 +/- 29 sec. The WIR and WOR were also significantly higher for PGLs (p<0.001). NSTs showed a more delayed

enhancement (TTP value: 233 ms). On DWI sequences, the mean ADC value for PGLs (1.17 ± 0.19 10^-3 mm2/s) was significantly different than the other tumor groups ($p<0.001$). The mean ADC was higher in NSTs (1.81 ± 0.28 10^-3 mm2/sec) ($p<0.001$). NSCC exhibited a lower ADC (0.95 ± 0.2 10^-3 mm2/s) compared to PGLs. No differences in DCE-derived indices or ADC were observed between sporadic versus S*DHx*-mutated PGLs.

3.4 Discrimination of HNPGL with multivariate modeling

A distinct PGL group without overlap from other tumors was observed on principal component analysis using WIR, WOR, TTP and ADC **(Figure 3)**. NSTs and NSCCs were also separated from both each other and PGLs using the same criteria. A multiparametric classification and CART approach was used to determine optimal cut-off values to differentiate tumor groups. This method permitted to draw a decision tree **(Figure 4).** The analysis of DWI and pooled DCE MRI sequences resulted in a model **(Table 4).**

4. Discussion

Multiparametric MRI is known to be an added value in the diagnostic strategy of soft tissue tumors (e.g. parotid space tumors). Until now, very few studies with limited cases have evaluated quantitative parameters of DCE MR imaging in the diagnosis of parapharyngeal tumors.

Paragangliomas are rare tumours with a unique metabolism leading to neovascularisation, particularly rich in arterioles. SDHx mutations are found in up approximately 50% of HNPGL and are associated with metabolic changes that constitute an emerging metabolic hallmark of these tumors. These mutations lead to a disruption of Tricarboxylic Acid (TCA) cycle (also called Krebs cycle) with subsequent accumulation of succinate that alter various cellular and extra-cellular functions. Succinate acts as an oncometabolite an influences a broad spectrum of pathways such as the hypoxic response. Thus, the major outcome of elevated succinate levels is HIF stabilization despite normal oxygen supply (e.g., pseudohypoxia) that promotes tumor angiogenesis [9].

During the past 15 years, MRA has shown excellent results for localizing PGLs [6,10–14]. Overall, CE-MRA and T1-weighted sequence proved to be excellent in the detection HNPGLs with a sensitivity of 88.7 % and a specificity of 93.7 %. DWI has also shown high sensitivity for identifying PGL in the setting *SDHB*-related syndromes [15].

Beyond its detection and localization value, MR is also more likely to provide better characterization of tumors. Previous studies evaluating multiparametric MR imaging have focused on the use of either DCE or DWI imaging features alone. Furukawa *et al.,* evaluated the diagnostic efficacy of a time intensity curve analysis on DCE MRI for characterization of head and neck tumors (including a single case of PGL) in a cohort of 20 patients [16]. They

found that metastatic tumors had a significantly lower relative maximum enhancement and prolonged time to peak with lower relative WOR compared to benign lesions. Gaddikeri *et al.,* compared the imaging features of DCE-MRI in 2 PGLs and 4 schwannomas [8]. PGLs were characterized by a high peak enhancement and signal-enhancement ratio (equivalent to WIR in our study) and less time for maximum enhancement, whereas schwannomas had a lower peak enhancement and signal-enhancement ratio with more time for maximum enhancement. Yuan *et al.,* studied the features of HNPGLs on DWI and DCE-MRI [8]. The mean maximum enhancement ratio (equivalent to WIR) and TTP were estimated to be 193.79+/- 67.18 and 8.16+/- 3.29, respectively. DCE MRI was obtained with a fast spoiled gradient echo (FSPGR) acquisition technique. The better temporal resolution of this technique could explain the lowest TTP values compared to our findings. Sakai *et al.*, evaluated the value of non-contrast-enhanced 4D-MRA in head and neck tumors in comparison with contrast-enhanced 4D MRA. Time intensity curves were obtained for 3 PGLs, with the same patterns observed—a distinct peak followed by wash out. In our study, PGLs were characterized by a shorter time-to-peak intensity (TTP), and higher WIR and WOR compared to other groups [17].

Our study identifies a multiparametric MRI signature of HNPGLs in a large cohort of patients based on a combination of both DWI and DCE characteristics. We have deliberately chosen semi-quantitative parameters derived from the analysis of the time intensity curve. Such an approach is free of complex post-processing (e.g. arterial deconvolution) which allows it to be applicable in a multicentric setup.

Results from DWI-MRI are less common in the literature. The study from Yuan *et al.* found a mean ADC of 1.12 E-3 mm^2/s in a sample of 10 PGLs [6], which is concordant with

our results. A recent meta-analysis that included 1,227 lesions from 22 studies showed that ADC plays a limited role in distinguishing malignant from benign lesions in the head and neck region. The authors conclude that a mean ADC value greater than 1.75 E-3 mm2/s is in favour of a benign lesion [18]. However, this study is hampered by mixing a wide diversity of neoplasms located in various anatomical deep cervical spaces, and must be interpreted with caution. Indeed, miscellaneous lesions can frequently develop in parotid space where benign neoplasms (such as Whartin tumors) classically demonstrate diffusion restriction with low ADC values (usually below 1 E-3 mm^2/s). Furthemore, only 12 PGLs were included in this meta-analysis (10 without topographic specification and 2 glomus jugulare PGLs) and different DWI MR-techniques were performed. Therefore, the heterogeneity in tumor origin and DWI sequences along with the absence of anatomical-space based analyses are a potential sources of overlap between ADC-values that must be considered.

This study has some limitations. First, it is retrospective in nature. Different types of DCE sequences were used to assess quantitative parameters. GRE and 4D-DCE sequences have a better temporal resolution than SE-DCE, which explains the wide range in TTP values. An additional limitation is the lack of pathological confirmation (level 1 of evidence gold standard) for all tumors. However, the diagnosis of PGL can be made by ^{18}F-FDOPA PET/CT and can serve as so-called "*in vivo*" immunohistochemistry [19]. False positive results have been reported in only a few anecdotal case reports including solid pseudopapillary tumors of the pancreas, thyroid neoplasms of follicular origin (oncocytoma), squamous cell carcinomas (cervix, epiglottis), poorly differentiated adenocarcinomas and melanomas.

To our best knowledge, no previous study has examined the combination of DWI and DCE MR imaging in a large cohort of vascular space tumors. Our study shows that multiparametric MR plays an important role for tumor subtyping. Accurate characterization of these tumors by reliable imaging biomarkers could help to avoid unnecessary biopsies and

guide further investigation. Our results would need to be validated in the setting of a prospective study. After confirmation, the validated quantitative values could be implemented in softwares to allow for automated detection and classification of vascular space tumors.

5. Conclusion

This study identifies a multiparametric MRI signature of paragangliomas that provides a strong impetus for switching from qualitative to quantitative analysis of deep soft-tissue tumors of the neck. MR features may serve as biomarkers for HNPGL diagnosis which could prevent unnecessary biopsy sampling and guide further investigation.

6. Ethical approval

The study was approved by an institutional Ethics Advisory Committee for using anonymous personal data extracted from institutional medical datafiles for research purposes. Written informed consent was waived by the Institutional Review Board.

The author(s) declare that this manuscript has not been published previously and not under consideration for publication elsewhere.

7. Funding statement

The author(s) received no financial support for the research, authorship, and/or publication of this article.

8. CRediT authorship contribution statement

EA : Conceptualization, Methodology, Formal analysis, Writing. MM : Conceptualization, Resources. NF : Resources. JPL : Resources. KP : Conceptualization, Visualization. DT : Conceptualization, Methodology, Investigation, Writing. AV : Conceptualization, Methodology, Formal analysis, Writing.

9. Declaration of Competing interest

The authors declare no conflict of interest.

10. References

[1] I. Espinosa-Medina, E. Outin, C.A. Picard, Z. Chettouh, S. Dymecki, G.G. Consalez, E. Coppola, J.-F. Brunet, Parasympathetic ganglia derive from Schwann cell precursors, Science (80-.). 345 (2014) 87–90. https://doi.org/10.1126/science.1253286.

[2] M.E. Kastriti, P. Kameneva, D. Kamenev, V. Dyachuk, A. Furlan, M. Hampl, F. Memic, U. Marklund, F. Lallemend, S. Hadjab, L. Calvo-Enrique, P. Ernfors, K. Fried, I. Adameyko, Schwann Cell Precursors Generate the Majority of Chromaffin Cells in Zuckerkandl Organ and Some Sympathetic Neurons in Paraganglia, Front. Mol. Neurosci. 12 (2019). https://doi.org/10.3389/fnmol.2019.00006.

[3] A. Varoquaux, N. Fakhry, S. Gabriel, S. Garcia, A. Ferretti, S. Chondrogiannis, D. Rubello, D. Taïeb, Retrostyloid parapharyngeal space tumors: A clinician and imaging perspective, Eur. J. Radiol. 82 (2013). https://doi.org/10.1016/j.ejrad.2013.01.005.

[4] D. Taïeb, A. Kaliski, C.C. Boedeker, V. Martucci, T. Fojo, J.R. Adler, K. Pacak, Current Approaches and Recent Developments in the Management of Head and Neck Paragangliomas, Endocr. Rev. 35 (2014) 795–819. https://doi.org/10.1210/er.2014-1026.

[5] A. Archier, A. Varoquaux, P. Garrigue, M. Montava, C. Guerin, S. Gabriel, E. Beschmout, I. Morange, N. Fakhry, F. Castinetti, F. Sebag, A. Barlier, A. Loundou, B.

Guillet, K. Pacak, D. Taïeb, Prospective comparison of ^{68}Ga-DOTATATE and ^{18}F-FDOPA PET/CT in patients with various pheochromocytomas and paragangliomas with emphasis on sporadic cases, Eur. J. Nucl. Med. Mol. Imaging. 43 (2016). https://doi.org/10.1007/s00259-015-3268-2.

[6] G. Gravel, P. Niccoli, V. Rohmer, G. Moulin, F. Borson-Chazot, P. Rousset, A. Pasco-Papon, C. Marcus, F. Dubrulle, H. Gouya, F. Bidault, B. Dupas, J. Gabrillargues, A. Caumont-Prim, A. Hernigou, A.-P. Gimenez-Roqueplo, P. Halimi, The value of a rapid contrast-enhanced angio-MRI protocol in the detection of head and neck paragangliomas in SDHx mutations carriers: a retrospective study on behalf of the PGL.EVA investigators*, Eur. Radiol. 26 (2016) 1696–1704. https://doi.org/10.1007/s00330-015-4024-5.

[7] R. Aschenbach, S. Basche, T.J. Vogl, J. Klisch, Diffusion-Weighted Imaging and ADC Mapping of Head-and-Neck Paragangliomas, Clin. Neuroradiol. 19 (2009) 215–219. https://doi.org/10.1007/s00062-009-9004-1.

[8] S. Gaddikeri, D.S. Hippe, Y. Anzai, Dynamic Contrast-Enhanced MRI in the Evaluation of Carotid Space Paraganglioma versus Schwannoma, J. Neuroimaging. 26 (2016) 618–625. https://doi.org/10.1111/jon.12351.

[9] S. Nölting, N. Bechmann, D. Taieb, F. Beuschlein, M. Fassnacht, M. Kroiss, G. Eisenhofer, A. Grossman, K. Pacak, Personalized management of pheochromocytoma and paraganglioma, Endocr. Rev. (2021). https://doi.org/10.1210/endrev/bnab019.

[10] J.-C. Ferré, J.-F. Brunet, B. Carsin-Nicol, A. Larralde, B. Godey, J.-Y. Gauvrit, Optimized time-resolved 3D contrast-enhanced MRA at 3T: Appreciating the feasibility of assessing cervical paragangliomas, J. Neuroradiol. 37 (2010) 104–108. https://doi.org/10.1016/j.neurad.2009.08.004.

[11] F. Neves, L. Huwart, G. Jourdan, D. Reizine, P. Herman, E. Vicaut, J.P. Guichard,

Head and Neck Paragangliomas: Value of Contrast-Enhanced 3D MR Angiography, Am. J. Neuroradiol. 29 (2008) 883–889. https://doi.org/10.3174/ajnr.A0948.

[12] R. van den Berg, A. Schepers, F.T. de Bruïne, L. Liauw, B.J.A. Mertens, A.G.L. van der Mey, M.A. van Buchem, The value of MR angiography techniques in the detection of head and neck paragangliomas, Eur. J. Radiol. 52 (2004) 240–245. https://doi.org/10.1016/j.ejrad.2003.12.002.

[13] S.M. Arnold, R. Strecker, K. Scheffler, J. Spreer, J. Schipper, H.P.H. Neumann, J. Klisch, Dynamic contrast enhancement of paragangliomas of the head and neck: evaluation with time-resolved 2D MR projection angiography, Eur. Radiol. 13 (2003) 1608–1611. https://doi.org/10.1007/s00330-002-1717-3.

[14] M.F. Mafee, B. Raofi, A. Kumar, C. Muscato, GLOMUS FACIALE, GLOMUS JUGULARE, GLOMUS TYMPANICUM, GLOMUS VAGALE, CAROTID BODY TUMORS, AND SIMULATING LESIONS, Radiol. Clin. North Am. 38 (2000) 1059–1076. https://doi.org/10.1016/S0033-8389(05)70221-9.

[15] N. Tufton, G. White, W.M. Drake, A. Sahdev, S.A. Akker, Diffusion-weighted imaging (DWI) highlights SDHB -related tumours: A pilot study, Clin. Endocrinol. (Oxf). (2019) cen.13980. https://doi.org/10.1111/cen.13980.

[16] M. Furukawa, U. Parvathaneni, K. Maravilla, T.L. Richards, Y. Anzai, Dynamic contrast-enhanced MR perfusion imaging of head and neck tumors at 3 Tesla, Head Neck. 35 (2013) 923–929. https://doi.org/10.1002/hed.23051.

[17] M. Sakai, T. Illies, N. Jerusel, S. Tateishi, M. Uchikoshi, J. Fiehler, Y. Watanabe, K. Nakanishi, N. Tomiyama, Feasibility of non-contrast-enhanced four dimensional (4D) MRA in head and neck tumors, comparison with contrast-enhanced 4D MRA, Springerplus. 5 (2016) 1282. https://doi.org/10.1186/s40064-016-2953-3.

[18] A. Surov, H.J. Meyer, A. Wienke, Apparent Diffusion Coefficient for Distinguishing

Between Malignant and Benign Lesions in the Head and Neck Region: A Systematic Review and Meta-Analysis., Front. Oncol. 9 (2019) 1362. https://doi.org/10.3389/fonc.2019.01362.

[19] D. Taïeb, R.J. Hicks, E. Hindié, B.A. Guillet, A. Avram, P. Ghedini, H.J. Timmers, A.T. Scott, S. Elojeimy, D. Rubello, I.J. Virgolini, S. Fanti, S. Balogova, N. Pandit-Taskar, K. Pacak, European Association of Nuclear Medicine Practice Guideline/Society of Nuclear Medicine and Molecular Imaging Procedure Standard 2019 for radionuclide imaging of phaeochromocytoma and paraganglioma, Eur. J. Nucl. Med. Mol. Imaging. 46 (2019) 2112–2137. https://doi.org/10.1007/s00259-019-04398-1.

Legends

Table 1: Patient, Lesion and Acquisition Characteristics in the Study Population

PGL: Paraganglioma, NSCC: Squamous Cell Carcinoma Metastatic Nodes, NST: Nerve Sheath Tumor, SE : Spin Echo Dynamic-Contrast Enhanced MR-Angiography, GE: Gradient Echo Dynamic-Contrast Enhanced MR-Angiography, 4D: 4D-MRA

Table 2: MR Imaging Acquisition Parameters

SE: Spin Echo Dynamic-Contrast Enhanced MR-Angiography, GE: Gradient Echo Dynamic-Contrast Enhanced MR-Angiography, 4D : 4D-MRA, DWI: Diffusion-Weighted Imaging

Table 3: Univariate analysis of quantitative MR parameters. Mean values and SD for ADC, TTP, WIR and WOR in each group

ADC: Apparent Diffusion Coefficient, TTP: Time to Peak, WIR : Wash In ratio, WOR : Wash Out Ratio, PGL: Paraganglioma, NSCC : Squamous Cell Carcinoma Metastatic Node, NST : Nerve Sheath Tumor

Table 4: Multivariate analysis of quantitative MR parameters: performances of regression tree (CART) method

Se: Sensibility, Sp : Specificity, PPV: Positive Predictive Value, NPV: Negative Predictive Value

Figure 1: Representative time intensity curves and images of paraganglioma (A, B, C, D), schwannoma (E, F, G, H), and squamous cell carcinoma metastatic lymph node (I, J, K, L).

A, E, I : DCE imaging enhancement time-intensity curves (x-axis represents time in seconds, y-axis signal intensity). PGL (A) demonstrates a peak initial enhancement with a short time-to-peak, and a rapid wash-out. Schwannoma (E) and NSCC (I) demonstrate a more progressive enhancement with a plateau phase (without wash out).

B, F, J : T2-weighted images in axial (B, F) and coronal (J) planes. PGL (B) demonstrates a typical heterogenous signal. Here the 'Salt and pepper' appearance is not obvious. Schwannoma (F) demonstrates a heterogenous appearance with hyperintense portions. Metastatic lymphadenopathy (J) demonstrates a lower signal compared to schwannoma.

C, G, K : Apparent diffusion coefficient map. PGL (C) and schwannoma (G) are moderately cellular lesions with ADC values of 1.2 and 1.3 x 10^-3 mm2/s respectively. NSCC (K) exhibits a lower ADC value (0.9 x 10^-3 mm2/s) compared to other tumors.

D, H, L : 4D-MRA acquisition at early (arterial) time. PGL (D) exihibits an intense enhancement whereas schwannoma (H) and lymphadenopathy (L) are not enhanced at early phase.

Figure 2: Box plots of quantitative perfusion and diffusion parameters

On the univariate analysis, all parameters are significantly different between NSCC, NST and PGL with a p-value < 0.001 for each parameter. ADC is significantly higher in NST

compared to PGL and NSCC. PGL exhibits significantly shorter TTP values, greater WIRs and WORs compared to NSCC and NST.

Figure 3: Clusters of quantitative variables constituting histological patterns

PCA provides a 2D overview of each patient's repartition according to the main quantitative parameters (ADC, TTP, WIR, WOR). Different clusters are determined with a : PGL, NSCC and NST. These groups are well separated without overlap, indicating that the quantitative parameters are able to differentiate between groups with remarkable accuracy.

Figure 4: Regression trees

The first predictor was ADC, which allows for the identification of NST when the value is higher than 1.65 (x 10^-3mm2/s). When the ADC-value is lower than 1.65, TTP is the second discriminating criteria. PGLs are eliminated with a high accuracy when the TTP is higher than 75.8 s. A short TTP (< 75.8 s) and an ADC-value that is higher than 0.97 are predictive of a PGL. When the TTP is short and the ADC < 0.97, the lesion can be either a PGL or NSCC.

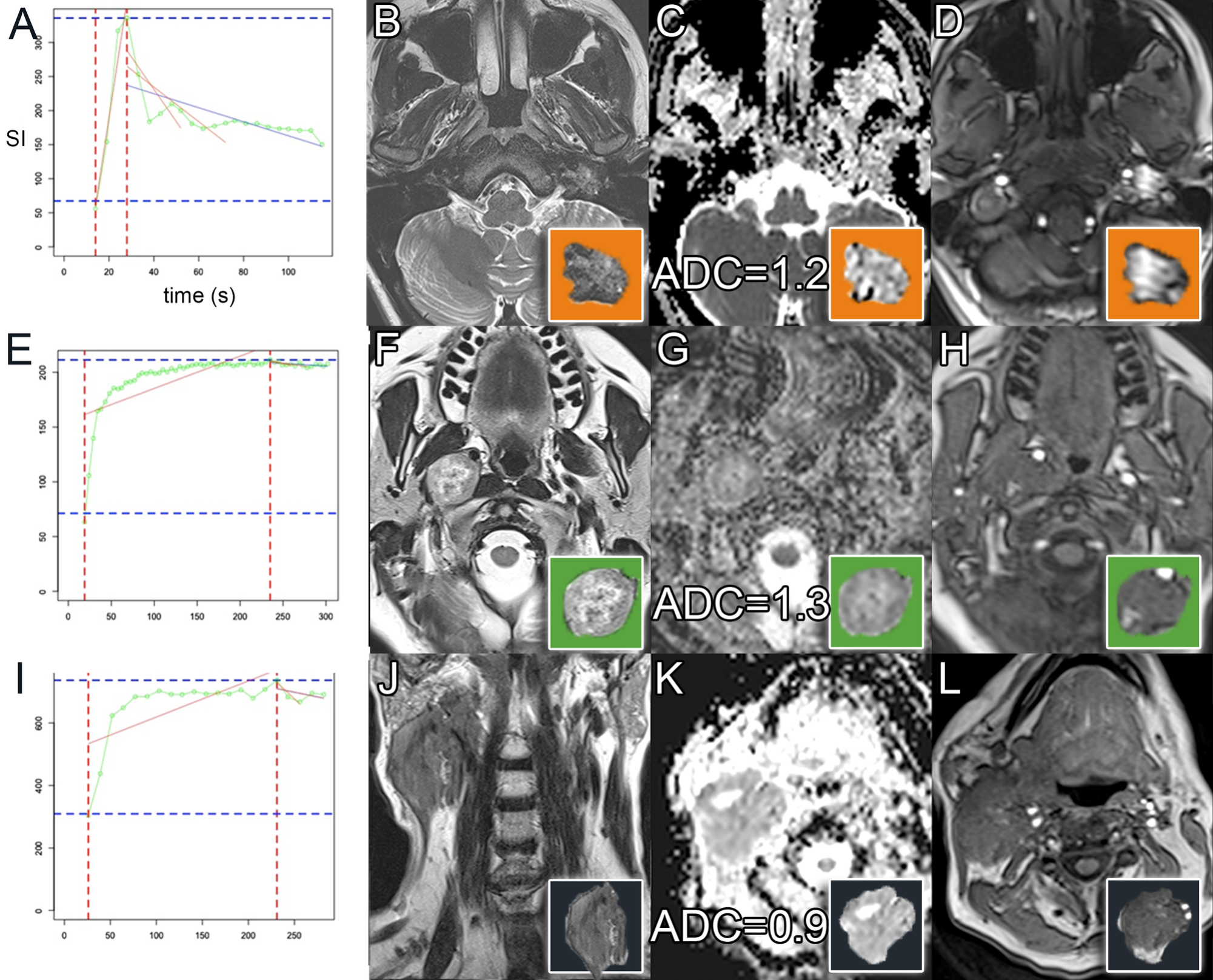
A
SI
time (s)
B
C
ADC=1.2
D
E
F
G
ADC=1.3
H
I
J
K
ADC=0.9
L

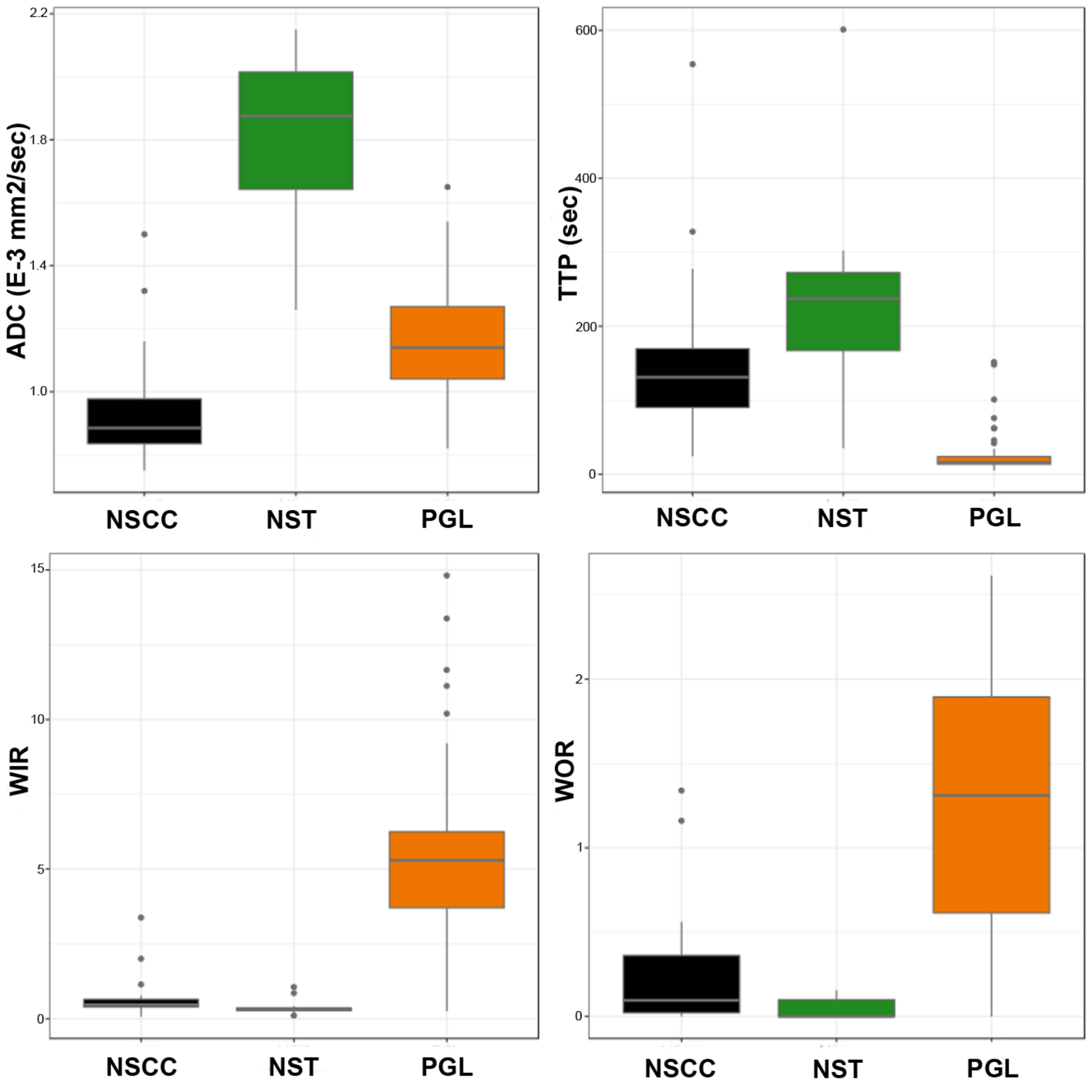
ADC (E-3 mm2/sec)
2.2
1.8
1.4
1.0
NSCC
NST
PGL
TTP (sec)
600
400
200
0
NSCC
NST
PGL
WIR
15
10
5
0
NSCC
NST
PGL
WOR
2
1
0
NSCC
NST
PGL

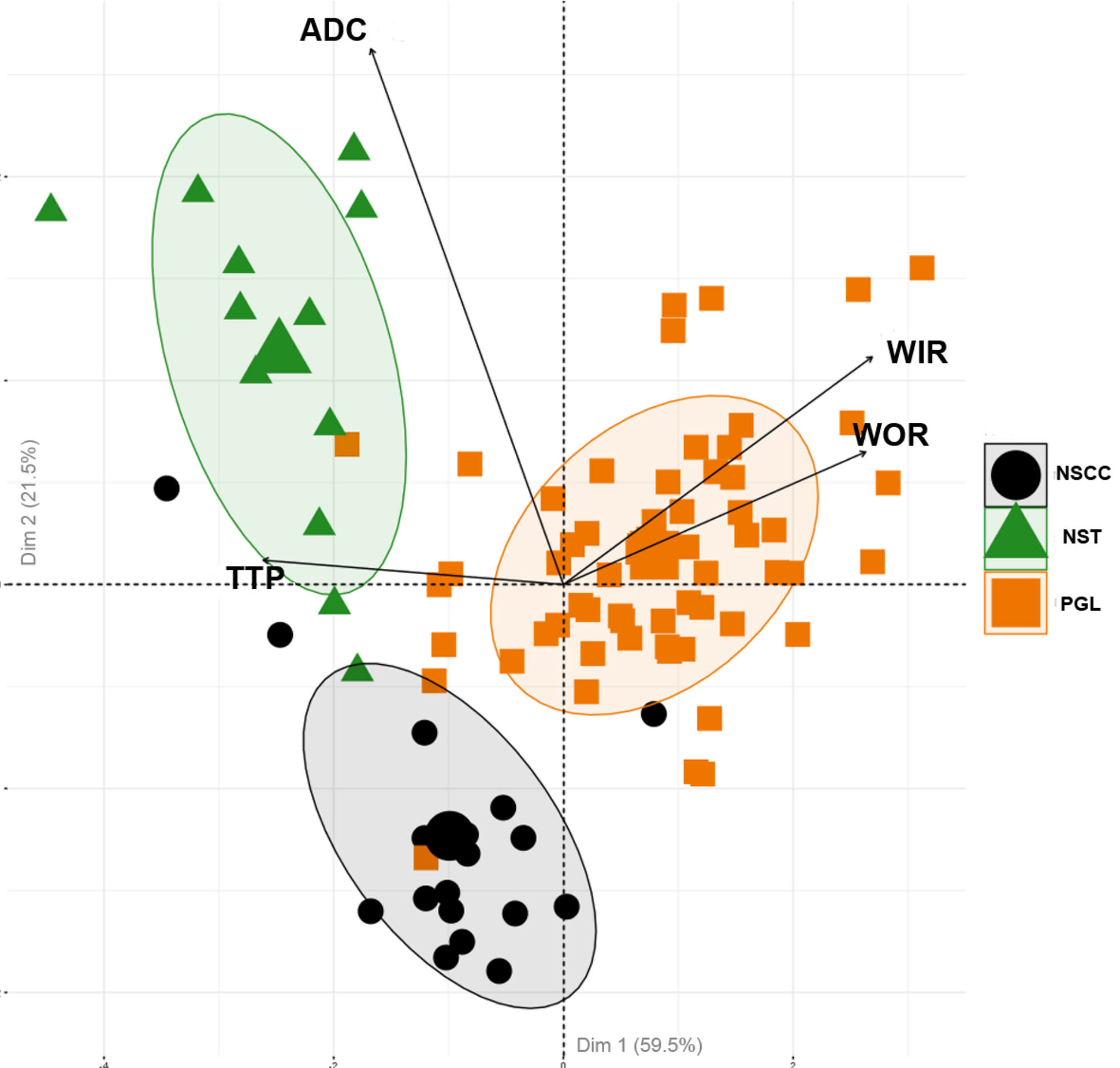
ADC
WIR
WOR
TTP
NSCC
NST
PGL
Dim 2 (21.5%)
Dim 1 (59.5%)

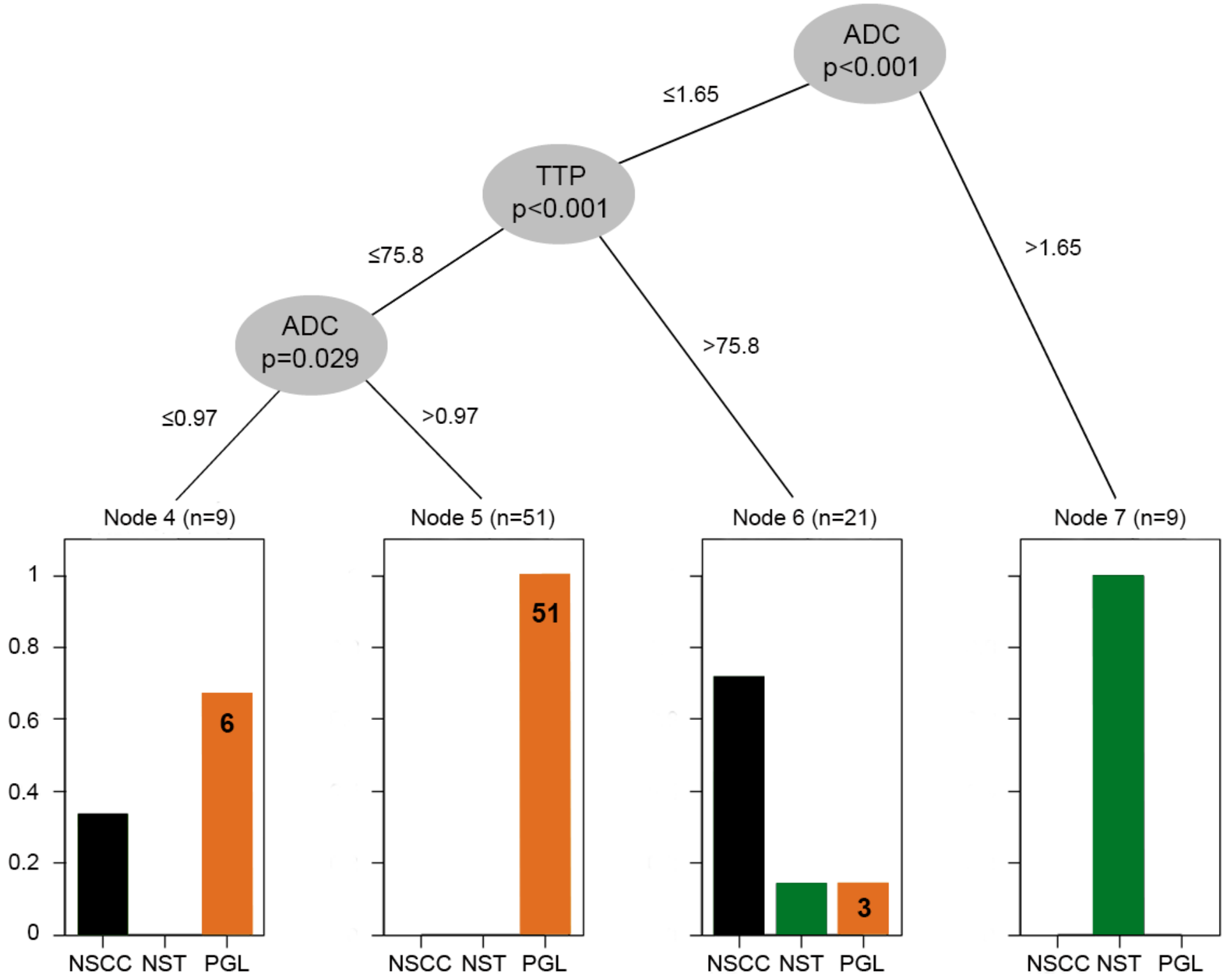
ADC
p<0.001
≤1.65
>1.65
TTP
p<0.001
≤75.8
>75.8
ADC
p=0.029
≤0.97
>0.97
Node 4 (n=9)
Node 5 (n=51)
Node 6 (n=21)
Node 7 (n=9)
1
0.8
0.6
0.4
0.2
0
6
51
3
NSCC NST PGL
NSCC NST PGL
NSCC NST PGL
NSCC NST PGL

Tables

Table 1.

	PGL	NSCC	NST
Number of patients	50	15	12
Number of lesions	60	18	12
Age (year)	58 ± 17	59 ± 16	77± 17
Gold standard			
Histology	28%	100%	33%
PET using a specific tracer	72%	0%	0%
Follow-up and consensus	0%	0%	67%
DCE-MRI methods			
SE	5%	94%	33%
GRE	40%	6%	50%
4D-ARM	55%	0%	17%

Table 2.

	SE	GE	4D	DWI
Acquisition plane	Axial	Axial	Coronal	Axial
Field of view (mm)	180 x 180	180 x 180	450 x 365	180 x 180
Matrix size	256 x 216	144 x 192	448 x 293	132 x 132
Slice thickness (mm)	5	4	2.5	4
Interslice gap (mm)	0.5	0	0	0.4
In plane resolution (mm)	0.7 / 0.83	1.25 / 0.94	1 / 1.25	1.36 x 1.36
TR/TE (ms)	300 / 11	5.47 / 1.85	2.95 / 1.1	4410 / 80
Flip angle (degrees)	166	15	30	180
b-values (s/mm2)				0, 100, 500, 1000
Temporal resolution	12.5 s	5 s	2.5 s	
Number of slices/ stack	7	12	40	
Acquisition time (sec)	300	300	150	

Table 3.

	PGL	SCC	NST	
	Mean ± SD	**Mean ± SD**	**Mean ± SD**	**p**
ADC	1.17 ± 0.19	0.95 ± 0.2	1.80 ± 0.29	<0.001
TTP	25.9 ± 29.30	160 ± 125	233.3 ± 145.3	<0.001
WIR	5.34 ± 2.99	0.72 ± 0.79	0.39 ± 0.28	<0.001
WOR	1.24 ± 0.80	0.27 ± 0.4	0.05 ± 0.06	<0.001

Table 4.

	n	CART	Se	Sp	PPV	NPV	Balanced Accuracy	p
PGL	60	ADC ≤ 1.65 & TTP ≤ 75.8	95%	90%	95%	90%	93%	p < 0.001
SCC	18	ADC ≤ 1.65 & TTP >75.8	83%	92%	71%	96%	88%	p < 0.001
NST	12	ADC > 1.65	75%	100%	100%	96%	88%	P < 0.001